

Anisotropic magnetic properties of the ferromagnetic semiconductor CrSbSe₃

Tai Kong, Karoline Stolze, Danrui Ni, Satya K. Kushwaha, and Robert J. Cava
Department of Chemistry, Princeton University, Princeton, NJ 08544, USA

Single crystals of CrSbSe₃, a structurally pseudo-one-dimensional ferromagnetic semiconductor, were grown using a high-temperature solution growth technique and were characterized by x-ray diffraction, anisotropic, temperature- and field-dependent magnetization, temperature-dependent resistivity and optical absorption measurements. A band gap of 0.7 eV was determined from both resistivity and optical measurements. At high temperatures, CrSbSe₃ is paramagnetic and isotropic with a Curie-Weiss temperature of ~ 145 K and an effective moment of $\sim 4.1 \mu_B/\text{Cr}$. A ferromagnetic transition occurs at $T_c = 71$ K. The a -axis, perpendicular to the chains in the structure, is the magnetic easy axis, while the chain axis direction, along b , is the hard axis. Magnetic isotherms measured around T_c do not follow the behavior predicted by simple mean field critical exponents for a second order phase transition. A tentative set of critical exponents is estimated based on a modified Arrott plot analysis, giving $\beta \sim 0.25$, $\gamma \sim 1.38$ and $\delta \sim 6.6$.

I. INTRODUCTION

Magnetic semiconductors have been studied for several decades for their potential applications in spintronics¹. Bulk materials like europium and chromium chalcogenides² are early examples of a ferromagnetic-semiconducting state, while ferromagnetism has also been successfully induced in well-developed semiconductors by magnetic doping^{3,4}. Another approach in spintronics is to deposit thin layers of a semiconducting ferromagnetic material on top of a non-magnetic material. Recently, there have been many attempts to control magnetism in 2-dimensional (2D) materials or topological insulators by proximitizing a ferromagnetic semiconductor^{5,6}. Several 2D magnetic semiconductors, CrGeTe₃ and CrI₃ in particular, have even been shown to maintain their ferromagnetism at an atomic-layer level⁷⁻⁹.

In the CrMX₃ ternary chromium tri-chalcogenides (where M is a non-transition-metal and $X = \text{S, Se, Te}$), the crystal structure varies depending on how CrX₆ octahedra are arranged. CrMTe₃ for $M = \text{Si, Ge and Sn}$, for example, have layered structure, with CrTe₆ octahedra forming a honeycomb lattice. When $M = \text{Sb, Ga}$, on the other hand, CrMX₃ compounds exhibit a pseudo-one-dimensional crystal structure, with CrX₆ octahedra forming infinite, edge-sharing, double rutile chains, and M atoms linking neighboring chains; for different M atoms, the relative angle between double rutile chains changes¹⁰. Among these pseudo-one-dimensional compounds, CrSbSe₃ is of interest due to its semiconducting ferromagnetic ground state. Previously, structural and magnetic properties have been reported for polycrystalline samples^{10,11}. Those studies showed that Cr in CrSbSe₃ appears as high-spin Cr³⁺, with $S = 3/2$ and that the material becomes ferromagnetic below ~ 70 K. To better understand the ferromagnetic properties of CrSbSe₃ and inspect the influence of structural low dimensionality on its magnetism, we present here electric transport and anisotropic magnetic properties of single crystalline CrSbSe₃.

II. EXPERIMENTAL METHODS

CrSbSe₃ single crystals were grown by crystallization from a Se-rich solution. Starting bulk elements were mixed in a molar ratio of Cr:Sb:Se = 7:33:60 and were sealed in an evacuated silica tube. The ampoule was then heated to 800 °C and slowly cooled to 680 °C, where the molten liquid was separated from the crystals in a centrifuge with silica wool serving as a filter. Remaining flux that attached to the surface of crystals were removed by keeping the crystal at 500 °C for 3 days in a sealed silica tube while leaving the cold end of the tube at room temperature. Millimeter-long single crystals of CrSbSe₃ are blade-like and malleable (see Fig.1(b)). Polycrystalline CrSbSe₃ was also synthesized, via solid state reaction. Starting elements in powder form were mixed in a stoichiometric ratio and sealed in an evacuated silica tube and were kept at 600 °C for 2 days.

Magnetization data were measured using a Quantum Design (QD) physical property measurement system (PPMS) Dynacool, equipped with a VSM option. Anisotropic magnetization data were obtained on selective pieces of single crystals. For field-dependent magnetization, when $H \parallel a$ and c , single crystals were mounted on a silica sample holder with GE varnish. For $H \parallel b$ and for polycrystalline sample, the standard QD plastic capsule was used. Because the mass of each single crystal is small, anisotropic magnetization measurements were normalized to the saturation magnetization values obtained on polycrystalline sample (which has a much larger mass) at 1.8 K. Anisotropic, temperature-dependent magnetization were measured on a shaft of samples, which only distinguish between $H \parallel b$ and $H \perp b$. Temperature-dependent resistivity was measured on a polycrystalline CrSbSe₃ pellet sample using the QD electrical transport option (ETO). Pt wires were attached to the sample via DuPont 4922N silver paint, using a two-probe configuration, suitable due to the very high resistance of the material.

Diffuse reflectance spectra were collected by a Cary 6000i UV-VIS-NIR spectrometer with an integrating

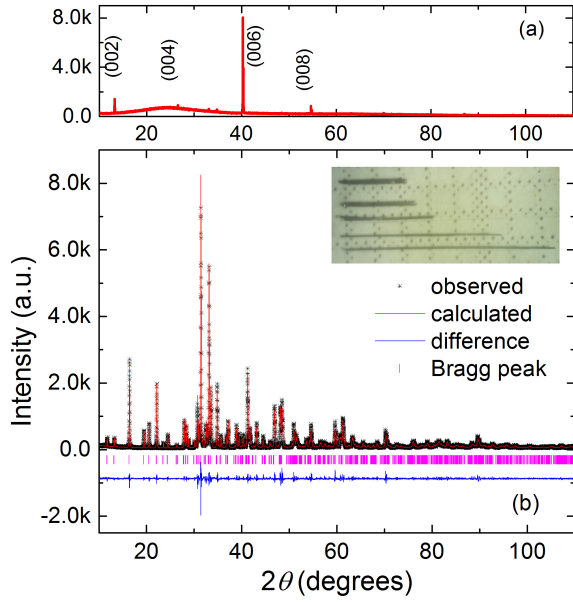


FIG. 1. (Color online) (a) Single crystal x-ray diffraction pattern along $(00l)$. (b) Powder x-ray diffraction pattern of CrSbSe_3 . Black crosses are measured data; red line shows the LeBail fitted curve; blue line indicates the difference between measured and calculated values; magenta ticks indicates the Bragg reflection positions. The inset shows several single crystals of CrSbSe_3 on a millimeter grid paper.

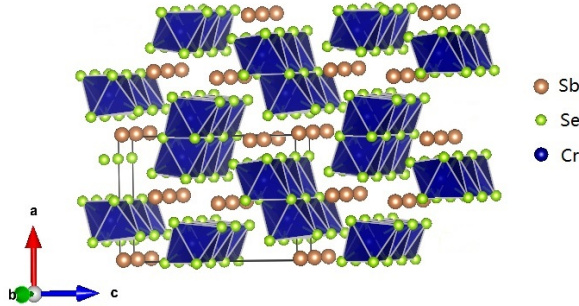


FIG. 2. (Color online) Crystal structure of CrSbSe_3 . CrSe_6 polyhedra are shown in blue.

sphere and were converted from reflectance to absorbance using Kubelka-Munk method. KBr was employed as the substrate. The sample for band gap measurement was mixed with KBr powder (sample to KBr, mass ratio 1:20) and pressed into a pellet. A pure KBr pellet with the same mass was prepared as the blank reference. Powder x-ray diffraction data were collected using a Bruker D8 Advance Eco, $\text{Cu K}\alpha$ radiation ($\lambda = 1.5406 \text{ \AA}$), equipped with a LynxEye-XE detector. The crystal structure of CrSbSe_3 was further determined by single-crystal x-ray diffraction (SXRD), which is presented in the Appendix.

III. RESULTS AND DISCUSSION

Powder x-ray diffraction data for CrSbSe_3 are shown in Fig. 1(b). All peaks can be indexed by the previously reported crystal structure, in agreement with our SXRD data^{10,11}. For single crystalline samples, the b -axis, is along the long crystal dimension¹⁰. The c -axis direction relative to the crystal morphology was determined from a single crystal laying on its flat face on a glass slide on a powder diffractometer. As shown in Fig. 1(a), these data show predominantly $(00l)$ peaks, indicating the c -axis is perpendicular to the blade-shaped sample. Minor peaks from other orientations may due to an imperfect alignment of the crystal on the glass slide.

The crystal structure of CrSbSe_3 is shown in Fig. 2. Edge sharing, slightly distorted, CrSe_6 octahedra form chains that extend along the b -axis. Each chain is composed of two parallel, edge sharing columns of CrSe_6 octahedra, forming double rutile chains. Between the chains, the Cr atoms are linked by two Se atoms; both Cr-Se-Cr angles are $\sim 92^\circ$. Sb atoms are located in between the double chains. Crystallographic data obtained from SXRD are summarized in Table I, final atomic parameters are listed in Table II and III in the Appendix.

The temperature-dependent resistivity of CrSbSe_3 is shown in Fig. 3. At 300 K, the resistivity is around $0.1 \text{ M}\Omega \text{ cm}$ and increases with decreasing temperature. When plotting resistivity as a function of inverse temperature on a semi-log plot, the resistivity shows a linear behavior, consistent with semiconducting behavior and a band gap of $\sim 0.7 \text{ eV}$. This band gap was also confirmed with optical absorbance measurements. In the inset of Fig. 3, the optical absorption coefficient as a function of wavelength is shown. A clear absorption edge is seen at around 1700 nm . The size of the band gap is estimated from this data to be $\sim 0.6 \text{ eV}$ based on an indirect band gap¹² model¹³, in agreement with our resistivity result. The measured band gap is slightly larger than the value calculated by DFT¹².

Fig. 4 shows the anisotropic magnetization of CrSbSe_3 as a function of temperature. In the paramagnetic state, the magnetic susceptibility of CrSbSe_3 appears to be nearly isotropic. A linear fit to the high temperature inverse magnetic susceptibility of the polycrystalline data gives an effective moment of $4.1 \mu_B/\text{Cr}$, which is slightly larger than the expected value for Cr^{3+} ($3.9 \mu_B/\text{Cr}$). The Curie-Weiss temperature extrapolated from the paramagnetic state is $\sim 145 \text{ K}$. A ferromagnetic transition occurs at around 70 K . Both the effective moment and Curie-Weiss temperature obtained in the current study agree with previously reported data for polycrystalline CrSbSe_3 samples^{10,11}.

Fig. 5 shows the anisotropic magnetization isotherm measured at 1.8 K . The demagnetization factor was estimated by assuming the geometry of the sample is close to a rectangular shape¹⁴. The internal field, H_{int} , was calculated from the relation $H_{int} = H - 4\pi NM$, where N is the demagnetization factor. For $H \parallel a$, which is

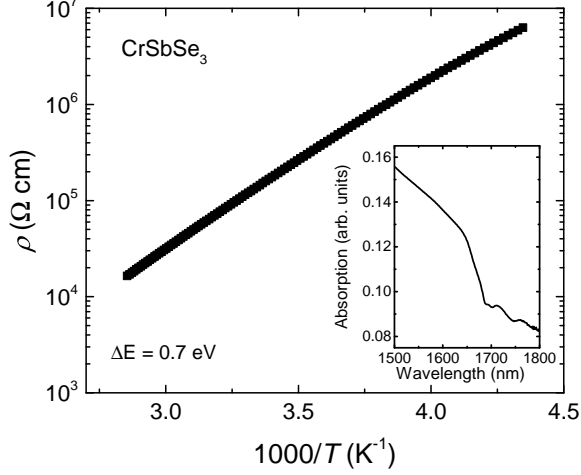


FIG. 3. Resistivity of CrSbSe₃ as a function of inverse temperature on a semi-log plot. Inset shows the optical absorption as a function of wavelength.

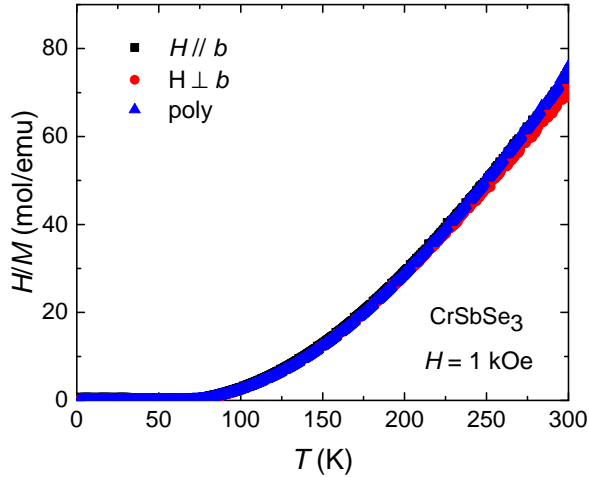


FIG. 4. (Color online) Anisotropic, temperature-dependent inverse magnetization of CrSbSe₃ measured at 1 kOe.

the easy axis, the demagnetization factor was also confirmed with the Arrott plot measured at around 2 K^{15,16}. Both demagnetization factor values are numerically similar. The value obtained from the Arrott plot along the *a*-axis was used to correct the calculated values for the other two orientations. As shown in Fig. 5, the *a*-axis, which is perpendicular to the chains, is the easy axis and the *b*-axis, the direction of the chains, is the hard axis, which saturates at ~15 kOe. The magnetization value saturates at 3 μ_B /Cr, consistent with expectations for $S = 3/2$ Cr³⁺.

To better determine the ferromagnetic transition temperature, we first considered the well-known Arrott

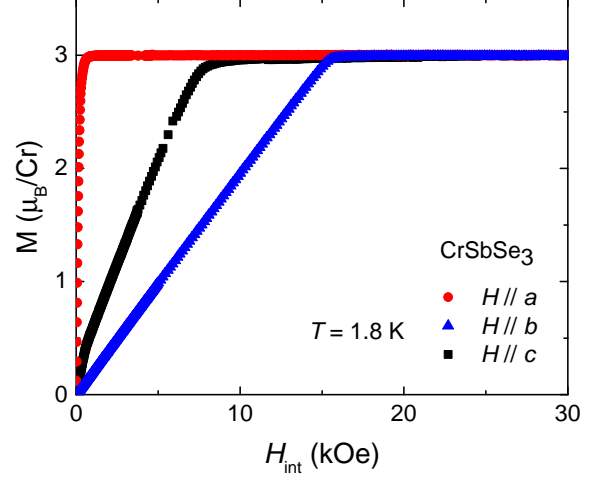


FIG. 5. (Color online) Anisotropic, field-dependent magnetization of CrSbSe₃ measured at 1.8 K. The CrSe₆ double rutile chains extend along the *b*-axis.

plot¹⁵. Magnetization isotherms along the easy axis were measured at various temperatures in the vicinity of the ferromagnetic transition temperature. M^2 as a function of H_{int}/M is displayed in Fig. 6(a). Because the Arrott plot describes the magnetic behavior at low fields in the proximity of T_c , only magnetization data below 25 kOe were considered. In the mean field description of the magnetization near T_c , curves in the Arrott plot should be a set of parallel straight lines with the one passing the origin indicating the ferromagnetic transition temperature. It is clear that the mean field critical exponent does not work for CrSbSe₃, as illustrated by a set of curved lines shown in Fig. 6(a).

For a second order phase transition, the spontaneous magnetization (M_s) below T_c , the initial magnetic susceptibility (χ_0^{-1}) above T_c and the field-dependent magnetization (M) at T_c are:

$$M_s(T) = M_0(-\epsilon)^\beta, \text{ for } T < T_c, \quad (1)$$

$$\chi_0^{-1} = (h_0/m_0)\epsilon^\gamma, \text{ for } T > T_c, \quad (2)$$

$$M = DH^{1/\delta}, \text{ for } T = T_c \quad (3)$$

where $\epsilon = (T - T_c)/T_c$; M_0 , h_0/m_0 , D are critical amplitudes; and β, γ, δ are critical exponents¹⁷. For the original Arrott plot, $\beta = 0.5$ and $\gamma = 1$ ¹⁵. In a more general case with different critical exponents, a modified Arrott plot is often considered, which formulates as:¹⁸

$$\left(\frac{H}{M}\right)^{1/\gamma} = a\epsilon + bM^{1/\beta} \quad (4)$$

where a and b are fitting constants. Since the mean field values apparently do not agree with our experimental data, we adopt the modified Arrott plot in order to better understand the nature of this ferromagnetic transition. In Fig. 6(b), we thus show the modified Arrott plot with a set of parameters ($\gamma = 1.38$, $\beta = 0.25$) that produces a set of straight lines satisfying the Arrott criteria. The ferromagnetic transition temperature, as depicted by the data that passes through the origin, is $T_c = 71$ K.

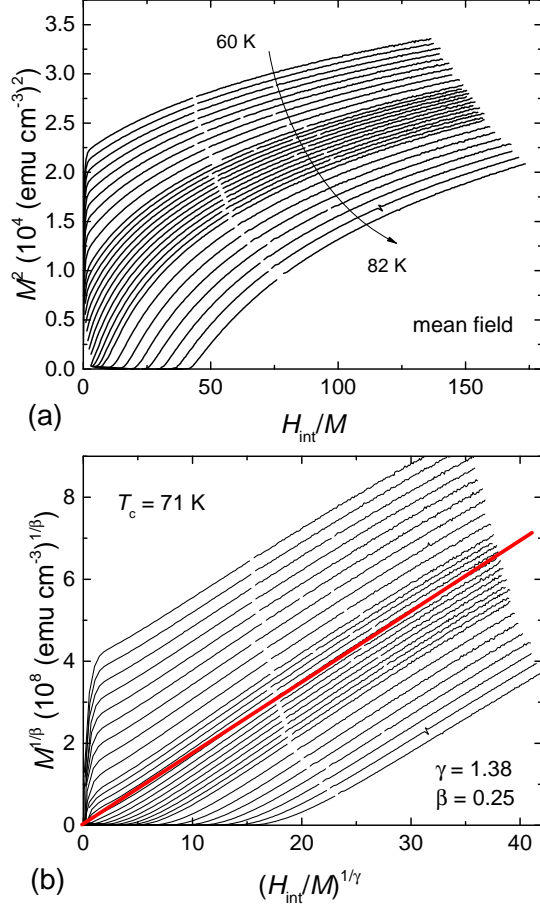


FIG. 6. (Color online) (a) Arrott plot with critical exponents from mean field theory ($\beta = 0.5$, $\gamma = 1.0$). (b) Modified Arrott plot with $\beta = 0.25$, $\gamma = 1.38$. Red solid line is a guide for the eyes, indicating the straight line that passes the origin at T_c .

In order to double-check the self-consistency of obtained critical exponents¹⁹, we extract the spontaneous magnetization and initial magnetic susceptibility from Fig. 6(b). The linearly extrapolated M_s and χ_0^{-1} are plotted as a function of temperature in Fig. 7(a). The solid curves are fitted lines according to Equation 1 and 2. The fitted critical exponent values are $\gamma = 1.39$ and $\beta = 0.26$, which are similar to the starting values. In the inset of Fig. 7(a), the field-dependent magnetization of CrSbSe₃ at $T_c = 71$ K is drawn on a log-log plot. According to Equation 3, the field dependence yield $\delta = 6.6$. In comparison to the theoretical prediction based on the

Widom relation²⁰:

$$\delta = 1 + \frac{\gamma}{\beta} \quad (5)$$

the calculated value of δ , using experimentally obtained critical exponents $\gamma = 1.38$ and $\beta = 0.25$, is ~ 6.5 , which agrees with what is obtained in Fig. 7(a).

The self-consistency can also be checked via the Kouvel-Fisher (KF) method²¹. According to the KF method,

$$\frac{M_s(T)}{dM_s(T)/dT} = \frac{T - T_c}{\beta} \quad (6)$$

$$\frac{\chi_0^{-1}(T)}{d\chi_0^{-1}(T)/dT} = \frac{T - T_c}{\gamma} \quad (7)$$

both $\frac{M_s(T)}{dM_s(T)/dT}$ and $\frac{\chi_0^{-1}(T)}{d\chi_0^{-1}(T)/dT}$ are linear function of temperature, with their slopes equal to the inverse of critical exponents. As seen in Fig. 7(b), linear lines are fitted to the experimental data and yield $\gamma = 1.36$, $\beta = 0.25$, again, very similar to the starting critical exponent values.

The self-consistency of these critical exponents indicates a good fit of the data with theoretical formalism. The set of critical exponents obtained is not close to any of the well-known theoretical values for various models. The values are also quantitatively different from that obtained for layered ternary chromium trichalcogenides^{22,23}. The use of the modified Arrott plot for fitting critical exponents is known to yield significant standard errors in some cases, which arises when choosing different field and temperature ranges for consideration. As a consequence, the standard errors are usually difficult to estimate, as has been discussed recently, for example, in CrGeTe₃^{22,23}, where slightly different criteria result in different critical exponent values. For the current study on CrSbSe₃, it is clear that the mean field critical exponents cannot describe the experimental data. The obtained critical exponents serve as a set of self-consistent values that matches our data, and may direct further detailed studies to a range around these values.

Finally, according to the Mermin-Wagner theorem, ferromagnetic or antiferromagnetic ordering cannot happen in ideal one- or two-dimensional systems at finite temperature within an isotropic Heisenberg model²⁴. In the case where magnetic anisotropy exists, however, this conclusion does not necessarily hold. In the case of CrSbSe₃, despite the fact that the magnetic-bearing sublattice of Cr³⁺ appears to be quasi-one-dimensional, the observed magnetic anisotropy in the ordered ferromagnetic state may contribute to its stability. Nevertheless, the obtained critical exponents still likely reflect the influence of low-dimensionality of the Cr³⁺ sublattice; further, more detailed investigation may be of interest.

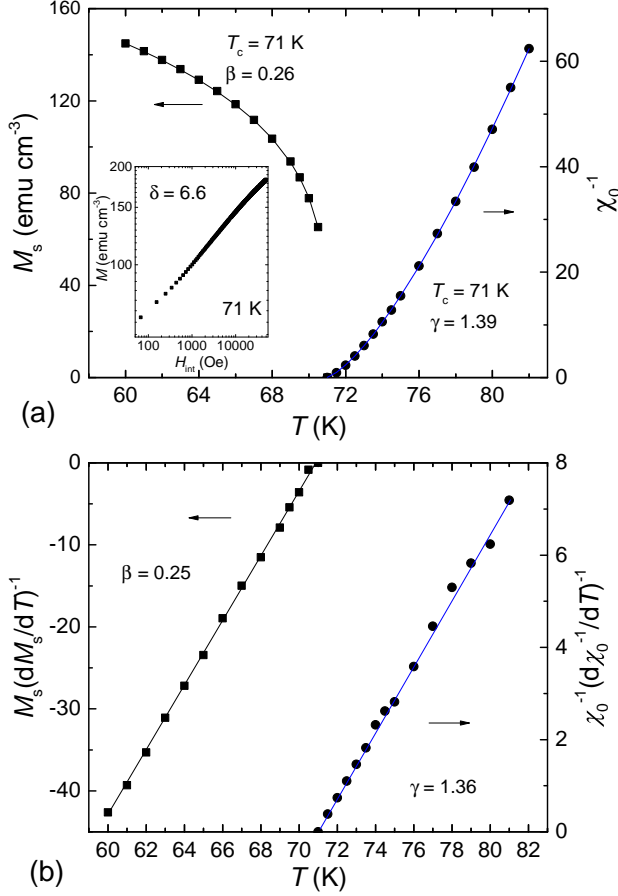


FIG. 7. (Color online) Temperature dependent spontaneous magnetization M_s and inverse initial magnetic susceptibility χ_0^{-1} . Inset shows the field-dependent magnetization data measured at $T_c = 71$ K on a log-log plot. (b) Kouvel-Fisher plots for $M_s(dM_s/dT)^{-1}$ and $\chi_0^{-1}(d\chi_0^{-1}/dT)^{-1}$. Solid lines are fitting curves to the data.

IV. CONCLUSIONS

In summary, we have synthesized CrSbSe₃ single crystals in a high-temperature, Se-rich solution and carried out a study on the structural, electrical and magnetic properties of that material. Structurally, CrSbSe₃ shows a pseudo-one-dimensional structure with magnetic-moment-bearing Cr sublattice forming double rutile chains. Electronically, CrSbSe₃ is a semiconductor with a band gap of ~ 0.7 eV. In its paramagnetic state, it appears to be magnetically isotropic with an effective moment of $\sim 4.1 \mu_B/\text{Cr}$ and a Curie-Weiss temperature of ~ 145 K. The ferromagnetic transition temperature was determined from a modified Arrott plot as $T_c = 71$ K. In the ferromagnetic state, CrSbSe₃ is anisotropic with the a -axis being the easy axis. Based on the modified Arrott plot and the Kouvel-Fisher method, we arrived at a set of critical exponents for second order phase transition that describe our experimental data: $\gamma = 1.38$, β

$= 0.25$ and $\delta = 6.6$. These values could serve as a starting point for further theoretical studies on magnetism at low-dimensions.

ACKNOWLEDGEMENTS

We would like to thank Valentin Taufour for insightful discussions and Tia S. Lee for experimental assistance. This work was supported by the Gordon and Betty Moore EPiQS initiative, grant number GBMF-4412.

APPENDIX

The SXRD data was collected at 296 K with a Kappa APEX DUO diffractometer equipped with a CCD detector (Bruker) using graphite-monochromatized Mo- K_α radiation ($\lambda = 0.71073$ Å). The raw data were corrected for background, polarization, and the Lorentz factor using APEX2 software²⁵, and a multi-scan absorption correction was applied²⁶. The structure was solved using the charge flipping method²⁷ and subsequent difference Fourier analyses with Jana2006^{28–30}. Structure refinement against F_o^2 was performed with Shelxl-2017/1^{31,32}.

TABLE I. Crystallographic data and details of the structure determination of CrSbSe₃ derived from single-crystal experiments measured at 296(1) K.

Sum Formula	CrSbSe ₃
Formula weight/(g mol ⁻¹)	410.63
Crystal system	orthorhombic
Space group	<i>Pnma</i> (no. 62)
Formula units per cell, <i>Z</i>	4
Lattice parameter <i>a</i> / Å	9.1388(3)
<i>b</i> / Å	3.7836(1)
<i>c</i> / Å	13.3155(4)
Cell volume/ (Å ³)	463.88(2)
Radiation	$\lambda(\text{Mo-}K_\alpha = 0.71073 \text{ Å})$ $2\theta \leq 82.23^\circ$
Data range	$-16 \leq h \leq 16, -6 \leq k \leq 6, -23 \leq l \leq 23$
Absorption coefficient/mm ⁻¹	31.5
Measured reflections	30213
Independent reflections	1527
Reflections with $I > 2\sigma(I)$	1379
<i>R</i> (int)	0.040
<i>R</i> (σ)	0.015
No. of parameters	31
<i>R</i> ₁ (obs)	0.017
<i>R</i> ₁ (all F_o)	0.022
<i>wR</i> ₂ (all F_o)	0.030
Residual electron density	1.12 to -0.98
(e ⁻ /Å ³)	

TABLE II. Wyckoff positions, coordinates, occupancies, and equivalent displacement parameters respectively for CrSbSe₃ single-crystal measured at 296(1) K. U_{eq} is one third of the trace of the orthogonalized U_{ij} tensor

Atom	Wyck. site	x	y	z	Occ.	U_{eq}
Sb1	4c	0.47058(2)	1/4	0/65793(2)	1	0.01332(3)
Cr1	4c	0.15547(4)	3/4	0.54468(3)	1	0.00701(5)
Se1	4c	0.28484(3)	3/4	0.71314(2)	1	0.01009(4)
Se2	4c	0.00186(2)	3/4	0.39112(2)	1	0.00784(4)
Se3	4c	0.32801(2)	1/4	0.48446(2)	1	0.00918(4)

TABLE III. Anisotropic displacement parameters for CrSbSe₃ single-crystal measured at 296(1) K. The coefficients U_{ij} ($/\text{\AA}^2$) of the tensor of the anisotropic temperature factor of atoms are defined by $\exp[2\pi^2(U_{11}h^2a^{*2} + \dots + 2U_{23}klb^*c^*)]$

Atom	U_{11}	U_{22}	U_{33}	U_{13}
Sb1	0.01182(6)	0.00899(6)	0.01915(7)	-0.00246(5)
Cr1	0.00735(12)	0.00616(12)	0.00752(13)	-0.00026(10)
Se1	0.01217(9)	0.00866(8)	0.00946(9)	-0.00064(7)
Se2	0.00848(8)	0.00777(8)	0.00726(8)	0.00029(7)
Se3	0.00937(8)	0.00815(8)	0.01001(9)	0.00127(7)

- ¹ I. Žutić, J. Fabian, and S. Das Sarma, Rev. Mod. Phys. **76**, 323 (2004).
- ² T. Dietl, Semicond. Sci. Technol. **17**, 377 (2002).
- ³ J. K. Furdyna, J. Appl. Phys. **64**, R29 (1988).
- ⁴ H. Ohno, Science **281**, 951 (1998).
- ⁵ Z. Wang, C. Tang, R. Sachs, Y. Barlas, and J. Shi, Phys. Rev. Lett. **114**, 016603 (2015).
- ⁶ H. Ji, R. A. Stokes, L. D. Alegria, E. C. Blomberg, M. A. Tanatar, A. Reijnders, L. M. Schoop, T. Liang, R. Prozorov, K. S. Burch, N. P. Ong, J. R. Petta, and R. J. Cava, J. Appl. Phys. **114**, 114907 (2013).
- ⁷ M.-W. Lin, H. L. Zhuang, J. Yan, T. Z. Ward, A. A. Puretzky, C. M. Rouleau, Z. Gai, L. Liang, V. Meunier, B. G. Sumpter, P. Ganesh, P. R. C. Kent, D. B. Geohegan, D. G. Mandrus, and K. Xiao, J. Mater. Chem. C **4**, 315 (2016).
- ⁸ C. Gong, L. Li, Z. Li, H. Ji, A. Stern, Y. Xia, T. Cao, W. Bao, C. Wang, Y. Wang, Z. Qiu, R. J. Cava, S. G. Louie, J. Xia, and X. Zhang, Nature **546**, 265 (2017).
- ⁹ B. Huang, G. Clark, E. Navarro-Moratalla, D. R. Klein, R. Cheng, K. L. Seyler, D. Zhong, E. Schmidgall, M. A. McGuire, D. H. Cobden, W. Yao, D. Xiao, P. Jarillo-Herrero, and X. Xu, Nature **546**, 270 (2017).
- ¹⁰ V. Volkov, G. V. Tendeloo, J. V. Landuyt, S. Amelinckx, E. Busheva, G. Shabunina, T. Aminov, and V. Novotortsev, J. Solid State Chem. **132**, 257 (1997).
- ¹¹ D. A. Odink, V. Carteaux, C. Payen, and G. Ouvrard, Chem. Mater. **5**, 237 (1993).
- ¹² A. Jain, S. P. Ong, G. Hautier, W. Chen, W. D. Richards, S. Dacek, S. Cholia, D. Gunter, D. Skinner, G. Ceder, and K. a. Persson, APL Materials **1**, 011002 (2013).
- ¹³ A. Tarasova, L. Isaenko, V. Kesler, V. Pashkov, A. Yeliseyev, N. Denysyuk, and O. Khyzhun, J. Phys. Chem. Solids **73**, 674 (2012).
- ¹⁴ A. Aharoni, J. Appl. Phys. **83**, 3432 (1998).
- ¹⁵ A. Arrott, Phys. Rev. **108**, 1394 (1957).
- ¹⁶ T. N. Lamichhane, V. Taufour, S. Thimmaiah, D. S. Parker, S. L. Bud'ko, and P. C. Canfield, J. Magn. Magn. Mater. **401**, 525 (2016).
- ¹⁷ M. E. Fisher, Rep. Prog. Phys. **30**, 615 (1967).
- ¹⁸ A. Arrott and J. E. Noakes, Phys. Rev. Lett. **19**, 786 (1967).
- ¹⁹ A. K. Pramanik and A. Banerjee, Phys. Rev. B **79**, 214426 (2009).
- ²⁰ B. Widom, J. Chem. Phys. **41**, 1633 (1964).
- ²¹ J. S. Kouvel and M. E. Fisher, Phys. Rev. **136**, A1626 (1964).
- ²² G. T. Lin, H. L. Zhuang, X. Luo, B. J. Liu, F. C. Chen, J. Yan, Y. Sun, J. Zhou, W. J. Lu, P. Tong, Z. G. Sheng, Z. Qu, W. H. Song, X. B. Zhu, and Y. P. Sun, Phys. Rev. B **95**, 245212 (2017).
- ²³ Y. Liu and C. Petrovic, Phys. Rev. B **96**, 054406 (2017).
- ²⁴ N. D. Mermin and H. Wagner, Phys. Rev. Lett. **17**, 1133 (1966).
- ²⁵ APEX2, Version v2013.10., Bruker AXS Inc., Madison, Wisconsin, USA (2013).
- ²⁶ G. M. Sheldrick, *Sadabs: Area-Detector Absorption Correction*, Version 2014/5, Bruker AXS Inc. (2014).
- ²⁷ G. Oszlányi and A. Süto, Acta Crystallogr A **60**, 134 (2004).
- ²⁸ G. Oszlányi and A. Süto, Acta Crystallogr A **64**, 123 (2008).
- ²⁹ V. Petříček, M. Dušek, and L. Palatinus, *Jana2006, The crystallographic computing system*, Institute of Physics, Praha, Czech Republic (2014).
- ³⁰ V. Petříček, M. Dušek, and L. Palatinus, Z. Kristallog. Cryst. Mater. **229**, 345 (2014).
- ³¹ G. M. Sheldrick, Acta Crystallogr C **71**, 3 (2015).
- ³² G. M. Sheldrick, *SHELX2017, Programs for crystal structure determination*, Universität Göttingen, Germany (2017).